

Extraction of Singular Patterns from a Vector Field via Persistent Path Homology

Yu Chen, Hongwei Lin

Abstract—The extraction of singular patterns is a fundamental problem in theoretical and practical domains due to the ability of such patterns to detect the intrinsic characteristics of vector fields. In this study, we propose an approach for extracting singular patterns from discrete planar vector fields. Our method involves converting the planar discrete vector field into a specialized digraph and computing its one-dimensional persistent path homology. By analyzing the persistence diagram, we can determine the location of singularity and segment a region of the singular pattern, which is referred to as a singular polygon. Moreover, the variations of singular patterns can also be analyzed. The experimental results demonstrate the effectiveness of our method in analyzing the centers and impact areas of tropical cyclones, positioning the dip poles from geomagnetic fields, and measuring variations of singular patterns between vector fields.

Index Terms—vector field, singularity, singular pattern, digraph, persistent path homology.

I. INTRODUCTION

EXTRACTING singular patterns from vector fields is an important problem in theoretical and practical domains. Singular patterns can detect the intrinsic characteristics of vector fields, such as divergence (convergence) patterns corresponding to sources (sinks) and rotational patterns corresponding to center points or spiral sources (sinks). They are commonly found in various vector field analysis problems, including vortex features of electromagnetic fields, vortex features generated by water currents, and wind field features of tropical cyclones. Identifying and extracting these singular patterns from vector fields is crucial to theoretical understanding and practical applications [1], [2].

In practical scenarios, the explicit expression of the vector field is frequently unknown, and only the field vectors at certain uniformly sampled grid points are accessible. In such instances, these vector fields are considered discrete. Fig. 1 illustrates examples of discrete vector fields.

While there exists a long history of research on the extraction of singular patterns, classical numerical methods may encounter accuracy issues and lack the capability to compare differences between singular patterns. In this study, we propose a method to determine the position of singularities and segment regions of singular patterns. Moreover, we can analyze the variations of singular patterns of a time-varying vector field. Given that discrete vector fields are similar with grid-shaped digraphs, we convert the grid-sampled vector field

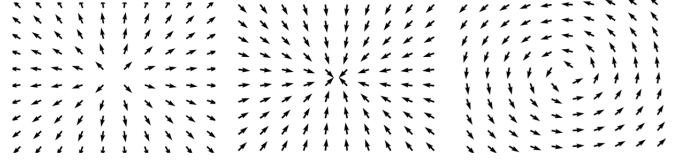


Fig. 1. Examples of discrete vector fields (left to right: divergence pattern, convergence pattern, and rotational pattern)

X into a specialized digraph and analyze its features using persistent path homology. Path homology [3], also known as GLMY homology, is a powerful tool for analyzing digraphs because it is sensitive to the directions in digraphs. Moreover, persistent path homology is a new perspective within the field of topological data analysis; it is specifically designed for analyzing digraph models. If a digraph contains intrinsic features conveyed by the direction and weight of its edges, these features can be discovered using (persistent) path homology.

Specifically, our method involves the following steps: First, we create a special digraph called an angle-based grid digraph from X and construct the corresponding digraph filtration. Then, the one-dimensional persistent path homology is computed to obtain the persistence diagram. Finally, the position of singularity can be determined, and a region of the singular pattern can be segmented, which we refer to as a *singular polygon*, based on the information provided by the persistence diagram. If a time-varying vector field is given, then we can also measure the changes in the topological features of the vector field by computing the distance between persistence diagrams. Moreover, in our experiments, the proposed method is employed to analyze tropical cyclones and geomagnetic fields by converting their planar vector field data into a digraph and subsequently extracting the corresponding singular patterns using persistent path homology.

In summary, the main contributions of our study are as follows:

- We develop a method to convert discrete vector fields into digraphs while preserving the information of the singular patterns.
- The positions of the singularities and the corresponding regions of singular patterns are determined by computing the one-dimensional persistent path homology of digraph filtrations.
- For a time-varying vector field, the variations can be measured by computing the distance between the corresponding persistence diagrams.
- Our method is successfully utilized to track two tropical

cyclones and position the Earth's dip poles.

The remainder of this paper is organized as follows: We provide an overview of persistent path homology and discrete vector field analysis in Section II. Then, we present a brief preliminary of vector field, digraph and path homology in Section III. The proposed method is introduced in Section IV and Section V. In Section VI we show our experiment results and provide a discussion. Section VII presents the conclusions and future works.

II. RELATED WORK

In this section, we provide an overview of persistent path homology and discrete vector field analysis. We first introduce persistent path homology and then discuss various methods for analyzing discrete vector fields, including the detection of singularities and the segmentation of singular patterns. Additionally, a brief introduction to comparing vector fields is provided.

A. Persistent Path Homology with Applications

Persistent homology is a powerful tool in topological data analysis for finding topological structures of data during filtration [4]–[6]. Path homology, proposed by Grigor'yan et al. [3], further extends the concept of persistent homology. It has been developed into various theories, such as homotopy theory for digraphs [7], discrete Morse theory on digraphs [8], and path homology theory of multigraphs and quivers [9]. Chowdhury and Mémoli [10] introduced the concept of persistent path homology of networks, which provides a new method for handling digraph models in the category of topological data analysis. Dey et al. [11] proposed an efficient algorithm for computing one-dimensional persistent path homology of digraph filtrations.

Path homology has found successful application in various practical problems. Chowdhury et al. [12] utilized path homology to investigate the structure of deep feedforward networks. Chen et al. [13] revealed intrinsic mathematical characteristics of molecules and materials by constructing directed networks and elucidated corresponding functional structures using persistent path homology. Liu et al. [14] proposed a structural characterization method based on path homology theory to extract structural information from materials and predict their properties. Wu et al. [15] employed path homology theory to analyze and interpret the topological changes in health states from symbiosis to dysbiosis and vice versa, identifying several hub metabolites and their interaction webs. In our study, we utilize one-dimensional path homology as the main tool to detect the singular patterns in the vector fields.

B. Discrete Vector Field Analysis

The study of discrete vector field topology has a long history, with numerous techniques available for analyzing vector field topology. Singularities and the flow curves or surfaces that connect them are classical tools for visualizing the topology of a vector field [16]. Additionally, various methods exist for addressing different types of singularities in

vector fields and analyzing their impact [17]–[20], providing different ways for visualizing vector fields. Moreover, vortices, which represent more general and physics-related features in vector fields and commonly appear in practical scenarios, can also be identified using a wide range of techniques designed for vector fields [21].

We now discuss methods for detecting singularities in discrete vector fields. If the expression of the vector field is known, the position of the singularity can be found by solving the system of equations [22]. However, this method is not applicable to discrete vector fields. Therefore, methods specifically designed for the discrete case have been proposed. One useful technique is Hodge decomposition [23], [24], which decomposes vector fields into three intuitive components: a divergence-free part, a curl-free part, and a harmonic part. Singularities can be detected using the decomposed vectors. Additionally, there are other numerical methods such as triangular linear interpolation of vectors [25] and the computation of the Jacobian matrix of the discrete vector field [26]. Moreover, Wong and Yip [1] introduced a method for finding the centers of circulating and spiraling vector field patterns by fitting a logarithmic spiral equation and modeling the field vectors for singular patterns corresponding to center points or spiral sources (sinks). Unlike certain numerical methods that may fail to find singularities or encounter spurious singularities caused by precision issues, thus demonstrating their limitations, this study proposes a method based on persistent path homology and an angle-based grid digraph for detecting singular patterns, relying on the singularity index.

Segmentation of discrete vector fields is important when we are interested in certain parts of a field that exhibit different patterns. Chen et al. [27] proposed a top-down approach of clustering vectors using certain similarity criteria to divide the vector field into several parts with their own features. Li et al. [2] proposed a method based on Hodge decomposition, Green function, and normalized cut to find the boundaries of regions with singular patterns. Zhang et al. [28] proposed a segmentation method that uses the accumulated geometric and physical attributes along integral curves to classify their behavior. Daniels et al. [29] introduced an interactive method for extracting vector field patterns based on the observation that although similar features in a vector field may differ spatially, they have similar neighborhood features. However, the boundary division of the singular pattern remains a significant challenge so far. In this study, we employ the theory of representative cycles of persistent path homology to segment regions of singular patterns.

Another issue arises in comparing vector fields from a topological perspective and measuring their differences, particularly investigating the variations of singular patterns in time-varying vector fields. Theisel et al. [30] introduced a topology-based comparison method that identifies changes in the singularities present in vector fields, serving as the primary method currently employed for comparing vector fields. Moreover, other topological features, such as closed orbits and separatrices, are also utilized in comparing vector fields at different moments in time-varying planar vector fields [25]. But these methods are hard to measure global variations

of singular patterns between vector fields. In our study, we utilize the distance between persistence diagrams to measure the topological variations of vector fields, particularly time-varying vector fields.

III. PRELIMINARIES

A. Concepts of Vector Fields

In the remainder of this paper, we focus on planar vector fields. We introduce some basic concepts about planar vector fields, which exhibit important topological properties. References on vector field properties can be found in [22].

Definition 1. (Singularity) Given a planar vector field $X = (P(x, y), Q(x, y))$ defined on $D \subseteq \mathbb{R}^2$, then a *singularity* $(x_0, y_0) \in D$ of X is a point such that $P(x_0, y_0) = Q(x_0, y_0) = 0$.

Singularity is an important concept of vector fields because it can determine the topologies of vector fields. From the perspective of the flow field or dynamical system, we can classify singularities into different types, such as *saddle*, *source*, *sink*, *center point*, *spiral source*, and *spiral sink* [22].

Definition 2. (Winding number) Suppose a simple closed curve L does not contain the singularities of the vector field $X = (P, Q)$. The *winding number* of X with respect to the curve L is defined as

$$j = \frac{1}{2\pi} \oint_L d \arctan \frac{Q}{P} = \frac{1}{2\pi} \oint_L \frac{P dQ - Q dP}{P^2 + Q^2}.$$

Here, the direction of the curve integral on L is counterclockwise.

Definition 3. (Index of a singularity) Suppose a simple closed curve L does not contain the singularities of the vector field $X = (P, Q)$, and the region surrounded by L only contains the unique singularity $S(x_0, y_0)$ of the vector field X , then the winding number of X with respect to the curve L is defined as the *index* of this singularity S .

Without causing confusion, the winding number of a curve is also called the *index of the curve*.

Theorem 1. [22] The winding number of a simple closed curve that encloses several singularities is the sum of the respective indices of those singularities. Thus a simple closed curve that encloses no singularity has index 0.

Theorem 2. [22] Suppose X is a vector field created by piecewise linear interpolation of a discrete vector field, then the index of a singularity of X is either 1 or -1 . If we regard X as a two dimensional systems, then a singularity has index -1 if and only if it is a saddle.

A precise definition for singular patterns, even for basic patterns such as vortices, does not exist [31]. However, given that singular patterns are characterized by the surrounding flow field of singularity, we define the *region of singular pattern* in Section IV through the properties of the angle-based digraph of the field. Moreover, we define the *singular polygon* in Section IV to represent a region of the singular pattern.

B. Digraph and Its Path Homology

Definition 4. (Digraph) A *digraph* is an ordered pair $G = (V, E)$, where V is a set of all vertices and E is a set of ordered pairs of vertices, i.e. directed edges that satisfy $E \subseteq V \times V$. If $G = (V, E)$ does not contain any loop and multiple edge, it is called a *simple digraph*.

Now we introduce the path homology of digraphs. The theories of path homology of general path complexes can be found in previous works [3].

Definition 5. (Elementary n -path and boundary operator) Let V be an arbitrary nonempty finite set whose elements are called vertices. For $n \geq 0$, an elementary n -path $i_0 \dots i_n$ on V is a sequence of $n + 1$ vertices in V . For $n = -1$ the set of elementary n -path is empty set \emptyset . An *elementary n -path* $i_0 \dots i_n$ is also denoted by $e_{i_0 \dots i_n}$. The boundary operator is defined as

$$\partial e_{i_0 \dots i_n} = \sum_{k=0}^n (-1)^k e_{i_0 \dots \hat{i}_k \dots i_n}$$

where the hat \hat{i}_k means omission of the index i_k .

An elementary path $e_{i_0 \dots i_n}$ on a set V is *regular* if $i_{k-1} \neq i_k, \forall k = 1, \dots, n$. Otherwise it is *non-regular*. Thus, using the vertex set of a simple digraph, we can obtain the set of elementary n -paths of G , where all elements are regular paths. In the following discussion, unless otherwise noted, simple digraphs are considered.

Definition 6. (Allowed n -paths) Let $G = (V, E)$ be a simple digraph, for any $n \geq 0$, the \mathbb{K} -linear space $\mathcal{A}_n(G) = \mathcal{A}_n(V, E; \mathbb{K})$ is defined as

$$\mathcal{A}_n = \mathcal{A}_n(G) = \text{span} \{e_{i_0 \dots i_n} : i_0, \dots, i_n \in V, i_k i_{k+1} \in E\}$$

where $k = 0, 1, \dots, n - 1$. The elements of \mathcal{A}_n are called *allowed n -paths*.

Definition 7. (∂ -invariant n -paths) Let $G = (V, E)$ be a simple digraph, for any $n \geq -1$, we define a subspace of \mathcal{A}_n as:

$$\Omega_n = \Omega_n(G) = \{v \in \mathcal{A}_n : \partial v \in \mathcal{A}_{n-1}\}$$

Here ∂ is the boundary operator, and we define $\Omega_{-1} = \mathcal{A}_{-1} \cong \mathbb{K}$ and $\Omega_{-2} = \mathcal{A}_{-2} = \{0\}$. The elements of Ω_n are called *∂ -invariant n -paths*.

Definition 8. (Path homology groups of digraph) Let $G = (V, E)$ be a digraph, and we have the following chain complex of V denoted as $\Omega_*(V) = \{\Omega_n\}$,

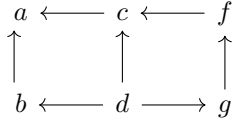
$$\dots \xrightarrow{\partial} \Omega_3 \xrightarrow{\partial} \Omega_2 \xrightarrow{\partial} \Omega_1 \xrightarrow{\partial} \Omega_0 \xrightarrow{\partial} \mathbb{K} \xrightarrow{\partial} 0,$$

and the associated *n -dimensional path homology group* of $G = (V, E)$ is defined as:

$$H_n(G) = H_n(V, E; \mathbb{K}) := \text{Ker}(\partial|_{\Omega_n}) / \text{Im}(\partial|_{\Omega_{n+1}})$$

The elements of $Z_n := \text{Ker}(\partial|_{\Omega_n})$ are called *n -cycles*, and the elements of $B_n := \text{Im}(\partial|_{\Omega_{n+1}})$ are called *n -boundaries*. A *representation* of a generator of $H_n(G)$ is an n -cycle in G but not an n -boundary. Usually it is not unique.

Example 1. Consider the following digraph:



There are five allowed 2-paths $e_{dba}, e_{dca}, e_{dgf}, e_{fca}, e_{gfc}$ that generate \mathcal{A}_2 . But there is only one ∂ -invariant 1-path $e_{dba} - e_{dca}$ that generates Ω_2 , since

$$\begin{aligned}
 \partial(e_{dba} - e_{dca}) &= e_{ba} - e_{da} + e_{db} - (e_{ca} - e_{da} + e_{dc}) \\
 &= e_{ba} + e_{db} - e_{ca} - e_{dc} \in \mathcal{A}_1.
 \end{aligned}$$

Now consider cycles $C_1 = e_{db} + e_{ba} - e_{ca} - e_{dc}$ and $C_2 = e_{dg} + e_{gf} + e_{fc} - e_{dc}$, then C_1, C_2 are cycles that generate Z_1 . But only C_1 is 1-boundary which generates B_1 , since $C_1 = \partial(e_{dba} - e_{dca})$. Hence, H_1 is generated by the class homologous to C_2 and $\dim H_1 = 1$.

Then we introduce the persistent path homology, which can be derived from classical persistent homology theory.

Definition 9. (One-dimensional persistent path homology [11]) Let $G = (V, E, w)$ be a weighted digraph where V is the vertex set, E is the edge set, and w is the weight function $w : E \rightarrow \mathbb{R}_+$. Denote $G^\delta = (V^\delta = V, E^\delta = \{e \in E : w(e) \leq \delta\})$, then we derive a *digraph filtration* $\{G^\delta \hookrightarrow G^{\delta'}\}_{\delta \leq \delta' \in \mathbb{R}_+}$ created by G . The *one-dimensional persistent path homology* of a weighted digraph $G = (V, E, w)$ is defined as the persistent vector space

$$\mathbb{H}_1 := \left\{ H_1(G^\delta) \xrightarrow{i_{\delta, \delta'}} H_1(G^{\delta'}) \right\}_{\delta \leq \delta' \in \mathbb{R}_+}$$

where $i_{\delta, \delta'} : G^\delta \hookrightarrow G^{\delta'}$ is the natural inclusion map. And G^δ is also called the *moment* corresponding to δ in the filtration.

In other words, a digraph filtration created by G can be defined as a subgraph sequence that retains all vertices of G and gradually adds edges of G in a non-decreasing order of weights.

A valuable tool for visualizing persistent homology is the *persistence diagram* (PD). The points (b_i, d_i) in the persistence diagram are referred to as *persistence pairs*, where b_i represents the birth time of a homology generator and d_i represents the death time of that homology generator. Fig. 2 illustrates an example of a persistence diagram. Moreover, various distances are used to quantify the dissimilarities of two persistence diagrams, such as bottleneck distance and Wasserstein distance [4], [32]–[34]. These distances can measure the topological differences between the original datasets. The persistence diagram can also be utilized to describe persistent path homology. We denote the one-dimensional path persistence diagram of \mathbb{H}_1 as $Dgm_1(G)$.

We now introduce a special kind of digraph, called the *cycle digraph*, which is useful when constructing a digraph from a vector field in the subsequent sections.

Definition 10. (Cycle digraph [3]) A digraph $G = (V, E)$ is a *cycle digraph* if it is connected (as an undigraph), and every vertex has the degree 2.

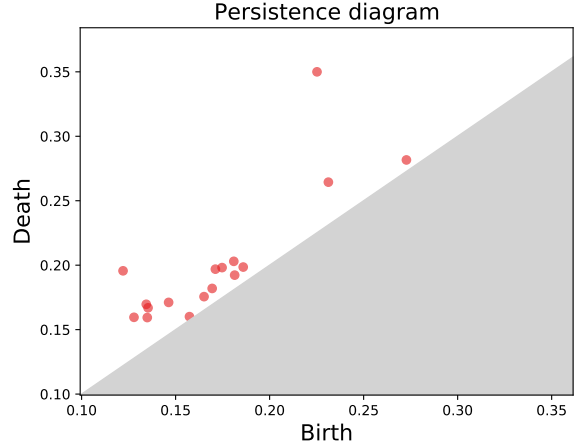


Fig. 2. Example of persistence diagram.

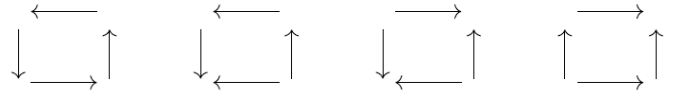
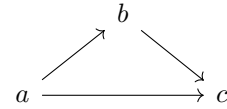


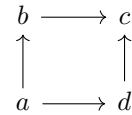
Fig. 3. Four kinds of squares, where only the rightmost one has a trivial one-dimensional homology group. We call the rightmost one boundary square and call the others non-boundary squares.

A *bigon* is a sequence of two distinct vertices $a, b \in V$ such that $a \rightarrow b, b \rightarrow a$.

A (*boundary*) *triangle* is a sequence of three distinct vertices $a, b, c \in V$ such that $a \rightarrow b, b \rightarrow c, a \rightarrow c$:



A (*boundary*) *square* is a sequence of four distinct vertices $a, b, c, d \in V$ such that $a \rightarrow b, b \rightarrow c, a \rightarrow d, d \rightarrow c$:



A bigon, a triangle, and a square are all cycle digraphs.

Theorem 3. (Path homology of a cycle digraph [3]) Let G be a cycle digraph. Then, $\dim H_p(G) = 0$ for all $p \geq 2$. If G is a bigon or a (*boundary*) triangle or a (*boundary*) square, then $\dim H_1(G) = 0$; otherwise, $\dim H_1(G) = 1$.

Consider a cycle digraph with only four vertices and four directed edges. Regardless of rotations and symmetries of the digraphs, which can be seen as having the same shape (for example, the following three digraphs:



), we focus solely on the directions of the edges. Consequently, such digraphs only have four distinct shapes, as depicted in Fig. 3. According to Theorem 3, only the rightmost shape exhibits a trivial one-dimensional homology group, leading us to refer to it as the

boundary square, whereas the remaining shapes are referred to as *non-boundary squares* [3], [11]. Throughout the subsequent discussion, when referring to the shape of a square (whether it is a boundary or non-boundary square), we disregard rotations and symmetries of the digraphs. In addition, when discussing a square, we consider it a digraph embedded in \mathbb{R}^2 . Thus, we are also interested in the interior area of the square.

Now, we focus on another type of cycle digraph, namely, the *polygon*, which consists of more than four vertices. Theorem 3 implies that all polygons possess non-trivial one-dimensional path homology groups, and the polygons themselves can serve as representations of the generators of these groups. Similar to squares, polygons are considered a digraph embedded in \mathbb{R}^2 , whose interior area is also considered.

The one-dimensional path homology of simple digraphs is clear because of the following Theorem 4. This theorem establishes the theoretical foundation for our subsequent exploration of the path homology of an angle-based grid digraph, which comprises boundary squares and non-boundary squares.

Theorem 4. [11] Let $G = (V, E)$ be a simple digraph. Let $Z_1 = \text{Ker}(\partial|_{\Omega_1})$, $B_1 = \text{Im}(\partial|_{\Omega_2})$, and let Q denote the space generated by all bigons and boundary triangles and boundary squares in G . Then, we have $B_1 = Q$. Hence the one-dimensional path homology group satisfies that $H_1 = Z_1/Q$.

IV. EXTRACTION OF SINGULAR PATTERNS FROM VECTOR FIELDS

In this section, we develop an algorithm for extracting singularities and obtaining the corresponding singular polygons. We first introduce the angle-based grid digraph, followed by the main algorithm and the analysis of its complexity.

The process of the developed method unfolds as follows: Initially, we choose a specific area and extract the corresponding vector field data. Then we construct an angle-based grid digraph, where each edge's weight is recorded. Subsequently, a digraph filtration is constructed by initially including all vertices of G and subsequently adding edges of G in a non-decreasing order of weights. This process enables the computation of the one-dimensional persistence diagram, thereby enabling the determination of the singularity's position and the extraction of the singular polygon, as outlined in Algorithm 1. If the vector field is time-varying, the changes of singular patterns can also be identified. The overall schematic of our methods is illustrated in Fig. 8. This systematic approach ensures a comprehensive analysis of the vector field data and facilitates the identification and characterization of singular patterns.

In the following discussion, we assume that the following conditions hold:

- (A1) In an angle-based grid digraph, any two vectors that are located on two adjacent points are not parallel. This conforms to most of the cases in practice.
- (A2) The singularities always have a positive index, i.e., saddles are not within our range of discussion.
- (A3) The singularity does not appear on an edge.

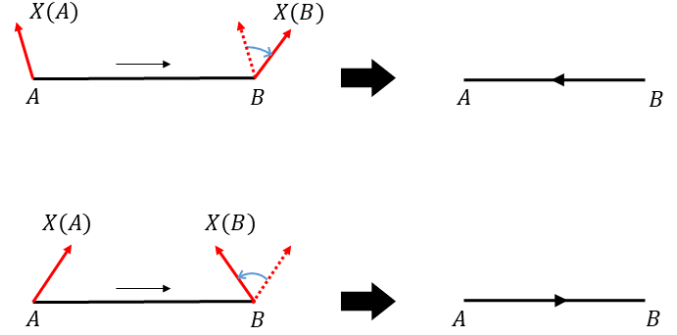


Fig. 4. (Top) The field vector rotates clockwise when moving along edge AB ; thus, the direction of AB is $B \rightarrow A$. (Bottom) The field vector rotates counterclockwise when moving along edge AB ; thus, the direction of AB is $A \rightarrow B$.

- (A4) The grid points are dense enough such that each smallest square encloses at most one singularity.

A. Constructing Angle-based Grid Digraph

We now introduce the primary tool used in this study, known as the *angle-based grid digraph*. As illustrated in Fig. 4, consider a given vector field X . Let $\mathbf{v}_A = X(A)$ and $\mathbf{v}_B = X(B)$ represent the vectors where X associates with points A and B , respectively. When we mention that a field vector \mathbf{v}_A rotates along AB to reach the field vector \mathbf{v}_B , we refer to the vector moving from point A to point B while concurrently undergoing rotation. This rotation occurs within the range of angles less than π . Specifically, if the rotation angle is less than π in the counterclockwise direction, we classify it as a counterclockwise rotation. Conversely, if the rotation angle exceeds π in the counterclockwise direction, the rotation is considered clockwise. Note that under assumption (A1), the angle magnitudes are not equal to π .

Let X be a discrete vector field defined on $D \subseteq \mathbb{R}^2$, sampled at uniform grid points where the distance between adjacent points in the horizontal or vertical direction is a constant $\varepsilon > 0$. We define $G(X, \varepsilon) = (V, E)$ as an *angle-based ε -grid digraph* created by X . When the parameter ε is clear from the context and does not cause confusion, we usually omit it and refer to $G(X)$ as the *grid digraph* in short. The vertex set V consists of all the sampling points of X on D , and E is the set of directed edges determined by the following rules (Fig. 4 and 5): for any two adjacent vertices A and B in V (i.e. the distance between A and B is exactly ε), if the field vector \mathbf{v}_A rotates counterclockwise along the line segment AB to reach the field vector \mathbf{v}_B , then the directed edge is defined as $A \rightarrow B$. Conversely, if the field vector \mathbf{v}_A rotates clockwise along the line segment AB to reach the field vector \mathbf{v}_B , then the directed edge is defined as $B \rightarrow A$. The weight of a directed edge AB is the absolute value of the rotation angle between the two vectors \mathbf{v}_A and \mathbf{v}_B . Additionally, no directed edges are found between non-adjacent vertices. Fig. 5 provides an example of an angle-based grid digraph created by a vector field.

According to assumption (A1), in the grid digraph G , no edge vanishing occurs between any two adjacent points.

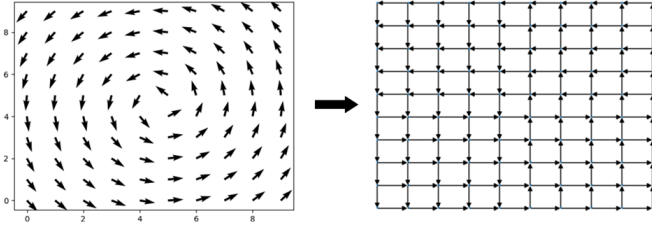


Fig. 5. Example of angle-based grid digraph created by a vector field. The vertices of the digraph are the exact points where vectors are sampled. If the left figure is a neighborhood of the singularity, then the corresponding grid digraph satisfies theorem 5.

Thus, the minimal cells of G consist of boundary squares and non-boundary squares. According to Theorem 4, the boundary squares in G generate $B_1(G)$. Consequently, the minimal generators of the one-dimensional path homology group $H_1(G)$ can be selected as all non-boundary squares in G .

Now we show that transformation from vector field into digraph can retain the information of singular patterns in the following theorem. The proof of this theorem is shown in the appendix.

Theorem 5. Let X be a discrete vector field with a singularity S . It follows that a neighborhood U of S exists, where when moving in a consistent direction along a horizontal or vertical line within U that does not intersect S , the field vector consistently rotates in the same direction. Consequently, let G be the corresponding angle-based ε -grid digraph; then, in G , the edges situated on the same horizontal or vertical line have same direction. Hence, the singular patterns of the vector field can be preserved in the digraph during the transformation process.

For example, as shown in Fig. 5, all edges of each horizontal and vertical line on the digraph have the same direction. According to the above theorem, when moving in the same direction along two horizontal or vertical lines on either side of the singularity, the direction of rotation of the field vectors are opposite. And U is a region that shows the features of the singular pattern. Thus we can define the region of the singular pattern through the property of the grid digraph above.

Definition 11. (Region of singular pattern) Suppose a vector field X exists with a singularity S ; if a neighborhood U of S satisfies the same condition as in Theorem 5, then U is called a *region of singular pattern* with respect to S .

B. Extracting Position of Singularity

After obtaining the grid digraph $G(X)$ created by the planar vector field X , our task can be simplified by identifying the squares that encompass the singularities of X . In this manner, we can limit our search to those specific squares to identify all the singularities through the computation of one-dimensional persistent path homology.

Let us begin by considering the closed piecewise linear

curve L represented by the diagram: $\begin{array}{ccc} D & \text{---} & C \\ | & & | \\ A & \text{---} & B \end{array}$. We as-

sume that L does not contain any singularities, and it can be denoted as $A \rightarrow B \rightarrow C \rightarrow D \rightarrow A$. The piecewise linear interpolation can be used to simplify the computation of the index of L if the vector field X is continuous [35]. Let $\mathbf{v}_1, \mathbf{v}_2, \mathbf{v}_3, \mathbf{v}_4$ represent the four vectors that X restricts on the four vertices A, B, C, D , respectively. The index of L is then given by the following equation:

$$\text{index}(L) = \frac{1}{2\pi} (\angle(\mathbf{v}_1, \mathbf{v}_2) + \angle(\mathbf{v}_2, \mathbf{v}_3) + \angle(\mathbf{v}_3, \mathbf{v}_4) + \angle(\mathbf{v}_4, \mathbf{v}_1)) \quad (1)$$

Here, $\angle(\mathbf{v}_i, \mathbf{v}_j)$ denotes the rotation angle from \mathbf{v}_i to \mathbf{v}_j , which lies in the range $(-\pi, 0) \cup (0, \pi)$. We define counterclockwise rotation angles as positive and clockwise rotation angles as negative, and the sampling points of the discrete vector field are assumed to be sufficiently dense, ensuring that the absolute values of the angles are less than π and not equal to zero.

Based on above discussions, the following theorem tells us that singularities can only exist in the interior area of non-boundary squares.

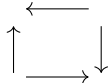
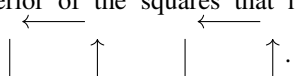
Theorem 6. Let G represent the angle-based grid digraph created by the vector field X , with each smallest square in G containing at most one singularity of X . We define S as the set of all smallest squares that encompass a singularity of X and T as the set of representations of minimum generators of the one-dimensional path homology group of G . In other words, T consists of all squares that have one of the following shapes: $\begin{array}{ccc} \leftarrow & & \rightarrow \\ \downarrow & \square & \uparrow \\ \rightarrow & & \leftarrow \end{array}$. It follows that $S \subseteq T$.

Proof. It is sufficient to prove that the singularities could not exist in the interior area of the boundary squares. Without loss of generality, let us consider the boundary square:


$\begin{array}{ccc} C & \text{---} & D \\ \uparrow & & \uparrow \\ A & \text{---} & B \end{array}$. According to the definition of the angle-based

grid digraph, when moving from A to B and from B to D , the vector undergoes a counterclockwise rotation, with the rotation angle ranging between $(0, \pi)$. Conversely, when moving from D to C and from C to A , the vector rotates clockwise, with the rotation angle ranging between $(-\pi, 0)$. By utilizing Equation (1), we observe that along the closed curve $ABDCA$, the sum of rotation angles falls within the range of $(-2\pi, 2\pi)$. Consequently, the number of revolutions made by the vector field X while traveling around the curve $ABDCA$ is zero because 0 is the only integer within the interval $(-1, 1)$. As stated in Theorem 1, this implies the absence of any singularities of X within the interior of the boundary square. \square

We can also prove that singularities of X could not exist in the interior of the squares that have the shape

. Thus, the singularities of X can only exist in the interior of the squares that have one of the following shapes:
 .

To extract the positions of singularities using one-dimensional persistent path homology, certain properties of singular patterns within a planar vector field X must be considered. If a singular pattern exists in X , it must satisfy the following properties:

Property 1. The smallest square in which the singularity is located must have a shape .

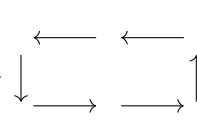
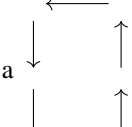
Proof. This property can be derived by Theorem 5 and Theorem 6 that the opposite edges of this square must have opposite directions. \square

Property 2. The smallest square containing a singularity must have an edge with the locally greatest weight.

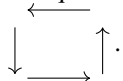
Proof. We can establish this property by considering the weights of the edges in a grid digraph, which correspond to the rotation angles between the vectors at their respective endpoints. Given that all edges in a grid digraph are of the same length, as shown by Theorem 5, as we approach the singularity, the field vector on an edge undergoes a faster rotation. Consequently, the rotation angle between the vectors at both ends of an edge increases as the edge gets closer to the singularity. Therefore, the weight of an edge is greater when it is closer to the singularity. Hence, the edge with the locally greatest weight must be part of the smallest square containing the singularity. \square

Property 3. Suppose G is a grid digraph generated by X . We compute the one-dimensional persistent path homology of the digraph filtration created by G , as defined in Definition 9. This computation yields a corresponding persistence diagram. If the selected region has only one singularity, then after adding the edge with the greatest weight, a new representation of the minimum generator of $H_1(G)$ containing the singularity emerges.

Proof. Before adding the edge with the greatest weight, according to Theorem 5, the representation containing the

singularity must be either a  or a .

configuration. Therefore, the edge with the greatest weight that is added last must be positioned in the middle of this hexagon. Regardless of the direction of the added edge, a new representation of the minimum generator of $H_1(G)$ emerges. Specifically, it is the smallest square that contains

the singularity, taking the shape of a . \square

In this property, the last square containing the singularity is formed by the edge with the greatest weight. Let the weight of this edge be denoted as a . This edge does not disappear in the digraph filtration, and therefore, it corresponds to a point $(a, +\infty)$ on the persistence diagram Dgm_1 . Consequently, we can identify all the points on Dgm_1 that take the form $(a_i, +\infty)$, indicating the points that persist until infinity. For each a_i and every edge in $G(X)$ with a weight of a_i , we examine the winding number of the adjacent smallest squares associated with this edge. The square with index 1 is what we are looking for.

Once the smallest square containing the singularity has been identified, we can determine the approximate position of the singularity based on the weights of the edges. While multiple approaches may be used to obtain the approximate coordinates, all edges evidently have the same weight, and the singularity should be located at the geometric center of the square. However, given that edges closer to the singularity possess greater weight, we can estimate the singularity's position using a weighting method. In this study, we utilize the concept of the *weighted center of the square* to approximate the singularity's coordinates, given by:

$$(x, y) = \left(\sum_{i=1}^4 \frac{w_i x_i}{w}, \sum_{i=1}^4 \frac{w_i y_i}{w} \right) \quad (2)$$

Here, (x_i, y_i) represents the midpoint coordinates of the four edges of the square, with corresponding weights w_i for $i = 1, 2, 3, 4$. The total weight is denoted as w , calculated as $w = \sum_{i=1}^4 w_i$. When considering two parallel edges within the square, the weight center is closer to the edge with a greater weight, similar to the singularity. Consequently, horizontally and vertically, the weight center and the singularity are positioned on the same side of the geometric center of the square. Therefore, if we use the notation ε to denote the length of the square's edges, the errors in the x and y coordinates between the weight center and the singularity are less than $\varepsilon/2$. The procedure for extracting the position of singularity is included in Algorithm 1 illustrated in subsection IV-D.

C. Segmenting the Region of Singular Pattern

Another crucial issue is the segmentation of a region exhibiting a singular pattern. For instance, when tracking a tropical cyclone, it is desirable to determine not only its central location but also the area it will impact. In our study, we utilize *singular polygons* as an approximation for delineating a region of the singular pattern. This concept is inspired by the methods used to extract representative cycles of the homology groups from classical persistent homology theory [36].

Let us revisit the definition of an angle-based digraph, where the edge weights in G represent absolute value of rotation angles. Considering the characteristics of singular patterns, we observe that the rotation angle between vectors at the ends of an edge diminishes as we move farther away from the singularity. Consequently, within the digraph filtration, in the vicinity of the singularity, the edge that is more distant from the singularity possesses a smaller weight and be added earlier than the closer edge.

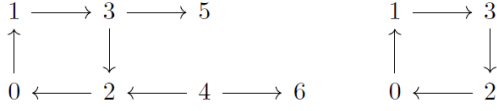


Fig. 6. The digraph on the right is the reduced digraph of the one on the left.

To streamline our discussion, we introduce the concept of a *reduced digraph*, which facilitates the examination of path homology within a digraph.

Definition 12. (Isolated edge) If an edge in graph G contains a vertex with degree 1, it is an *isolated edge* in graph G .

Definition 13. (Reduced digraph) Let G be a digraph, G_r is a subgraph of G , then we say G_r is a *reduced digraph* of G if G_r is the maximal subgraph of G that does not contain any isolated edges.

Theorem 7. [3] Suppose a graph G has a vertex a such that there is only one outgoing edge $a \rightarrow b$ from a and no incoming edges to a . Let $G' = (V', E')$ be the digraph with $V' = V \setminus \{a\}$ and $E' = E \setminus \{ab\}$. Then $H_p(G) \cong H_p(G')$ for all $p \geq 0$. The theorem still holds if we change the condition of edge to $b \rightarrow a$.

According to Theorem 7, a digraph and its reduced digraph have the same path homology group. For instance, in Fig. 6, the digraph on the right is the reduced digraph of the one on the left. Their path homology groups are identical. Therefore, if our focus is solely on the path homology of a digraph, we can equivalently study its reduced digraph.

Based on the preceding discussion, when adding the edges in a non-decreasing order of weight, there exists an edge that forms the minimum polygon encompassing the singularity we are seeking. In other words, after adding an edge e with weight $w(e)$, a new path homology generator is created, which can be represented by the minimum polygon containing e .

An example is shown in Fig. 7. On the left, a discrete vector field is depicted, showing a singular pattern generated by a singularity. On the right, four moments are selected from the reduced digraph filtration. The pink region in the second moment represents the minimum polygon encompassing the singularity, and the minimum polygon is situated within the region where the original vector field exhibits the singular pattern.

Definition 14 (Singular Polygon). The minimum polygon described above is referred to as the *singular polygon* corresponding to the singularity in X .

The singular polygon serves as a neighborhood of the singularity, illustrating the singular pattern.

We now discuss the process of obtaining the singular polygon using persistent path homology. When the aforementioned edge e is added, a new point $(w(e), +\infty)$ appears in Dgm_1 . Therefore, we can identify this edge by examining all the points in Dgm_1 in the form of $(a_i, +\infty)$. By traversing these points in non-decreasing order of the value of a_i , we can locate the edge e_i in G with weight a_i and analyze the reduced

digraph $G_r^{a_i}$. If $w(e)$ represents the minimum value at which the singular polygon appears in $G_r^{w(e)}$, then the corresponding edge e is responsible for the birth of this singular polygon. Once this edge e is identified, we record the singular polygon and draw the reduced digraph $G_r^{w(e)}$ to give a visualization of it. This process is also included in Algorithm 1.

D. Algorithm and Complexity Analysis

Now we present our algorithm for extracting singularities and singular polygons from a planar discrete vector field.

Algorithm 1 Extracting Singularity and Singular Polygon

Input: A planar discrete vector field X containing singularities.

- 1: Compute the grid digraph G from X .
- 2: Compute the persistence diagram $Dgm_1(G)$ using the one-dimensional persistent path homology of the digraph filtration created by G .
- 3: Let I be the set of points in $Dgm_1(G)$ of the form $(a_i, +\infty)$, and sort the elements in I in non-decreasing order of a_i .
- 4: **For** each point $(a_i, +\infty)$ in I **do**
 - For** each edge with weight a_i in G **do**
 - For** each adjacent smallest square to this edge **do**
 - Calculate the winding number of the square.
 - If** the winding number is 1 **then**
 - Compute the singularity (x, y) using Eq. (2).
 - End if**
 - End for**
 - End for**
- 5: **For** each point $(w, +\infty)$ in I **do**
 - If** G_r^w represents an earliest state in reduced digraph filtration forming a minimal polygon P with index 1 **then**
 - Record the polygon P .
 - End if**
- End for**

Return: The singularities and the corresponding singular polygons.

In analyzing the complexity of the Algorithm 1, we assume the input X has a rectangular grid of points with m points in each row and n points in each column (hence mn grid points in X in total), and in $Dgm_1(G)$ there are k points persist to $+\infty$. Note that k represents the number of non-boundary squares in G , thus is not greater than mn . We consider the time complexity of each steps. Step 1 has a complexity of $O(mn)$, which represents a linear relationship between the input sizes m and n . The computation persistent path homology of planar digraph in step 2 exhibits a complexity of $O((mn)^\omega)$ [11], where ω denotes the exponent of matrix multiplication, currently known to be less than 2.373. This step is particularly significant due to the high exponent, which can dominate the overall complexity for large input sizes. The sort process in step 3 has a complexity of $O(k \log k)$. Step 4 has a complexity of $O(kmn)$, but it does not exceed $O((mn)^\omega)$ since k is controlled by mn and is much smaller than mn in

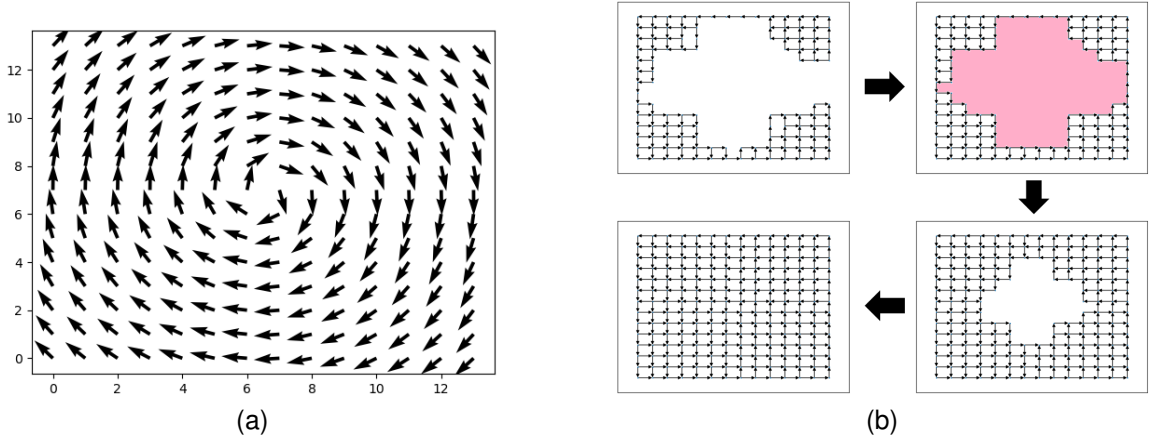


Fig. 7. (a) Example of a discrete vector field that has a singular pattern. (b) four selected moments in the reduced digraph filtration, where the pink region in the second one is the singular polygon corresponding to the singularity in the vector field on the left.

general cases. Lastly, in step 5, the complexity of searching the polygon P and computing its index is also $O(kmn)$, as it may repeat at most k times, and each search may involve traversing the entire grid to identify the polygon. Considering the relative magnitudes of these complexities, the step of computing persistent path homology with $O((mn)^\omega)$ stands out as the dominant term, determining the overall complexity of the algorithm. Therefore, if there are N grid points in X , the overall time complexity of Algorithm 1 is $O((N)^\omega)$.

V. DIFFERENCES MEASUREMENT OF VECTOR FIELDS

Our method also introduces a novel approach to compare the topology of two planar vector fields using persistent path homology theory. This involves computing the distances of 1-dimensional persistence diagrams obtained from two vector fields. Assuming two planar vector fields X_1 and X_2 are defined on the same domain, computing their respective 1-dimensional persistence diagrams PD_1 and PD_2 , and subsequently evaluating the corresponding distance $d(PD_1, PD_2)$ (here d represents the bottleneck distance or Wasserstein distance), allows us to measure the dissimilarity between the two persistence diagrams, thereby comparing the topological differences between X_1 and X_2 .

Moreover, when considering a time-varying vector field restricted to a fixed domain, we can track the variations in topology by sequentially computing the distance between two persistence diagrams obtained at two neighboring moments. A small distance between the persistence diagrams of neighboring moments suggests a minor variation in the singular pattern of the vector field, indicating greater stability during this period. Conversely, a large distance indicates a significant variation in the singular pattern of the vector field, indicating less stability during this period. This will be helpful to quantify and analyze changes in the vector field.

In practice, as we concentrate on the relative magnitude of the distances between persistence diagrams, using either the bottleneck distance or the Wasserstein distance can have a similar effect, given that the bottleneck distance can be considered as a special case of the Wasserstein distance.

Therefore, in the subsequent experiments, we employ the bottleneck distance as the primary measuring tool.

VI. EXPERIMENTS AND DISCUSSIONS

All the experiments in this section were conducted on a server equipped with a 2.90GHz Intel Core i7-10700 CPU and 16.0 GB RAM.

We will first present the experimental results obtained by using our method to track two tropical cyclones, namely Khanun and Saola, which emerged in 2023 and exhibited unusual trajectories. In this experiment, we use wind field datasets obtained from the Remote Sensing Systems Cross-Calibrated Multi-Platform's 6-hourly ocean vector wind analysis product on a 0.25 deg grid [37]; it is a gridded Level 4 (L4) product that provides vector wind over the world's oceans and provides gridded wind vector data at 4 times of day: 00:00Z, 06:00Z, 12:00Z, and 18:00Z (here Z stands for Universal Time Coordinated, UTC).

Various techniques can be used to detect the center of tropical cyclones [39]. For example, mathematical morphology operations applied to satellite cloud images [40]–[43], methods based on vector field [44]–[46] or scalar field [47], and AI-based methods utilizing satellite cloud images [48], [49]. These methods may involve multiple inputs and techniques, such as various dynamic and thermodynamic variables at different altitudes, and can be complex. In contrast, our method only utilizes wind field data to analyze rotational patterns and determine the center positions of cyclones, highlighting one of our advantages. Moreover, our method can also measure topological changes in tropical cyclones over time, demonstrating an additional advantage of the approach. Another experiment utilized the geomagnetic field datasets obtained from the International Geomagnetic Reference Field (IGRF) [38], a mathematical model describing the geomagnetic field and its changes, to determine the position of Earth's dip poles. Additionally, the algorithm proposed in [11] is used for computing one-dimensional persistent path homology.

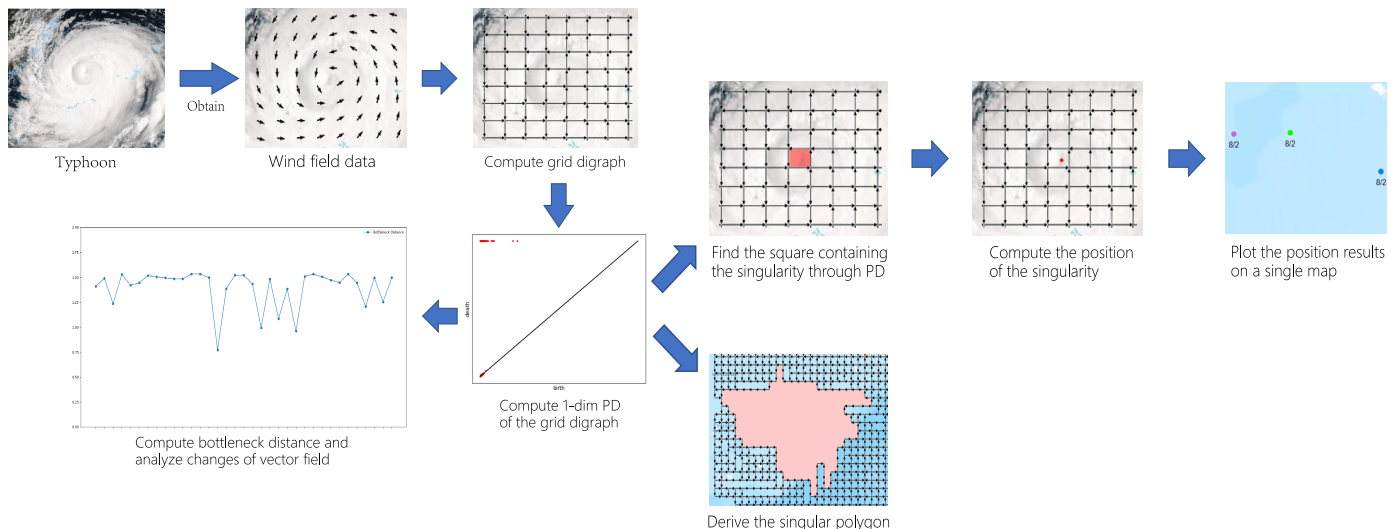


Fig. 8. Pipeline of our procedure. An illustrative example is presented, where we use the satellite cloud image of typhoon Khanun to display the wind field data of the area that is selected in our experiments.

A. Experiment Results of Extracting Singular Patterns

In the first experiment, we determine the centers of tropical cyclones based on the wind fields. Fig. 8 shows the pipeline of our procedure. As an illustrative example, we chose a specific local area from the wind field of typhoon Khanun. By processing the wind field data, we acquire the approximate latitude and longitude of the center positions of tropical cyclone for each provided moment. These positions are then plotted on a single map, as depicted in Fig. 9 (a) displays the positioning result for Khanun, whereas Fig. 9 (b) presents the positioning result for Saola. Each point on the map is labeled with the corresponding date, and the color indicates the observation time. The obtained positioning longitudes and latitudes for the centers of Khanun and Saola are presented in Table IV, alongside the actual longitudes and latitudes, as well as the errors. Here the actual positions of the tropical cyclones are obtained from the Regional Specialized Meteorological Center for Marine Meteorological Service, Beijing¹.

In addition, we compute the singular polygon that encompasses the center of a tropical cyclone and depict it in the corresponding reduced digraph. The wind field data from 2023-08-02-00:00 UTC is selected, covering a longitude range of 123.625°E–133.625°E and a latitude range of 21.125°N–31.125°N. The pipeline of our process is illustrated in Fig. 8. By executing Algorithm 1, we generate the digraph displayed in Fig. 10. In this figure, the singular polygon containing the center is highlighted in pink. Based on our previous discussion, this polygon should represent a region where the singular pattern exists, indicating the area influenced by the tropical cyclone Khanun. Considering that each pair of adjacent vertices is 0.25 degrees apart, we can determine, using the latitude-longitude to kilometer conversion formula²,

TABLE I
FOUR DIRECTION WIND CIRCLE RADIUS OF KHANUN AT
2023-08-02-00:00 UTC

| | NE | SE | SW | NW |
|-----------------------------|-------|-------|-------|-------|
| 7-level wind circle radius | 478km | 488km | 451km | 456km |
| 10-level wind circle radius | 262km | 231km | 176km | 207km |
| 12-level wind circle radius | 132km | 111km | 115km | 140km |

TABLE II
POSITIONING RESULTS OF MAGNETIC DIP POLES AND ERRORS

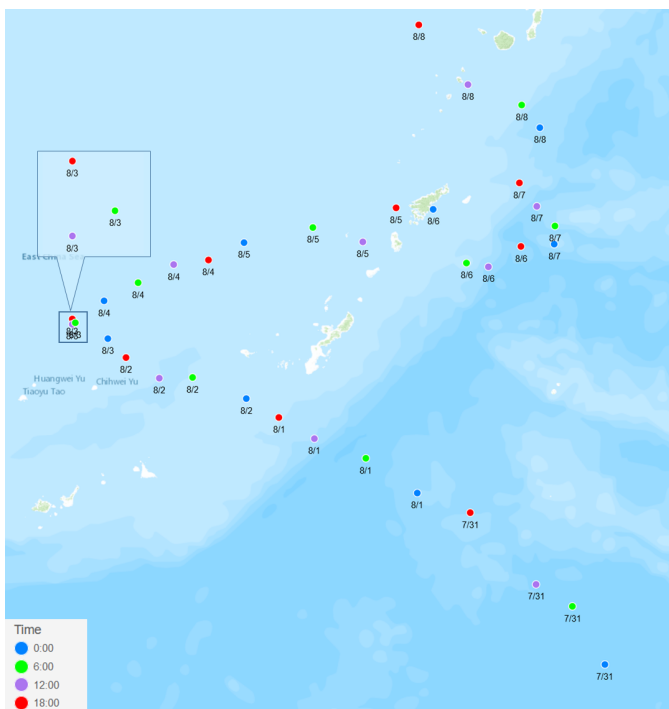
| North dip pole | | | | | | |
|----------------|-----------------------|----------------------|------------------|-----------------|---------------------|--------------------|
| Year | Positioning longitude | Positioning latitude | Actual longitude | Actual latitude | Errors of longitude | Errors of latitude |
| 2000 | 109.60°W | 80.91°N | 109.64°W | 80.97°N | 0.04° | 0.06° |
| 2005 | 118.13°W | 83.13°N | 118.22°W | 83.19°N | 0.09° | 0.06° |
| 2010 | 132.88°W | 85.12°N | 132.84°W | 85.02°N | 0.04° | 0.1° |
| 2015 | 160.37°W | 86.37°N | 160.34°W | 86.31°N | 0.03° | 0.06° |
| 2020 | 162.87°E | 86.39°N | 162.87°E | 86.49°N | 0° | 0.1° |
| South dip pole | | | | | | |
| Year | Positioning longitude | Positioning latitude | Actual longitude | Actual latitude | Errors of longitude | Errors of latitude |
| 2000 | 138.36°E | 64.64°S | 138.30°E | 64.66°S | 0.06° | 0.02° |
| 2005 | 137.88°E | 64.60°S | 137.85°E | 64.55°S | 0.03° | 0.05° |
| 2010 | 137.36°E | 64.39°S | 137.32°E | 64.43°S | 0.04° | 0.04° |
| 2015 | 136.63°E | 64.34°S | 136.60°E | 64.28°S | 0.03° | 0.06° |
| 2020 | 135.88°E | 64.12°S | 135.87°E | 64.08°S | 0.01° | 0.04° |

that P falls within the coverage of the tropical cyclone. This determination is supported by the data of wind circle radius shown in Table I, obtained from the Regional Specialized Meteorological Center for Marine Meteorological Service in Beijing. Thus, we confirm that the singular polygon represents a region where the singular pattern exists. However, given noise in the field, the shape of the singular polygon may exhibit some irregularity.

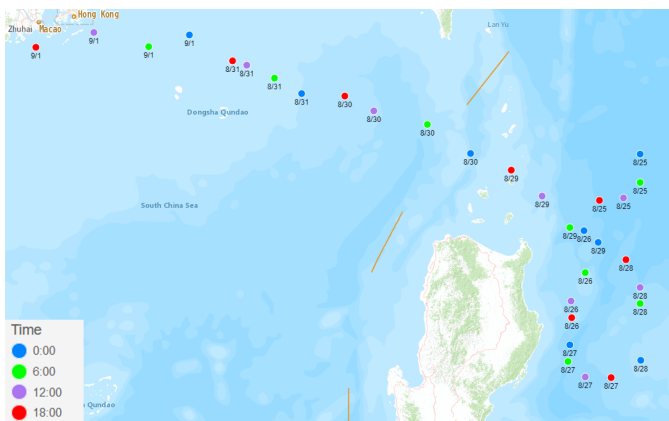
We also conducted another experiment in which we used projected geomagnetic field data to determine the location of the magnetic dip poles. The magnetic dip poles are defined as the locations where the main magnetic field as a whole is normal to Earth's surface, which provide a crucial reference

¹<http://eng.nmc.cn/typhoon/>

²For latitude, 1 deg \approx 110.574 km; for longitude, 1 deg \approx 111.320 \times cos(latitude) km



(a)



(b)

Fig. 9. Center tracking results of two typhoons. (a) Results of typhoon Khanun from 2023/07/31 to 2023/08/08. (b) Results of typhoon Saola from 2023/08/25 to 2023/09/01.

for local orientation when navigating on or close to Earth's surface at high-latitudes [38]. However, observations have shown that the positions of the two magnetic dip poles change from year to year [38], so it is necessary to calculate and update their positions in time. Our approach is well-suited to address this issue. When we project geomagnetic field data onto a map, resulting in a planar vector field, the two dip poles (north dip pole and south dip pole) become singularities of this planar vector field, since the projected vectors are zero at these points. In this experiment, we select two domains around the two dip poles respectively and choose geomagnetic field data at zero altitude. After projecting onto the map, discrete vector fields sampled around the two dip poles are obtained. Using our method, we determine the locations of the two dip poles for the years 2000, 2005, 2010, 2015, and 2020, and compare

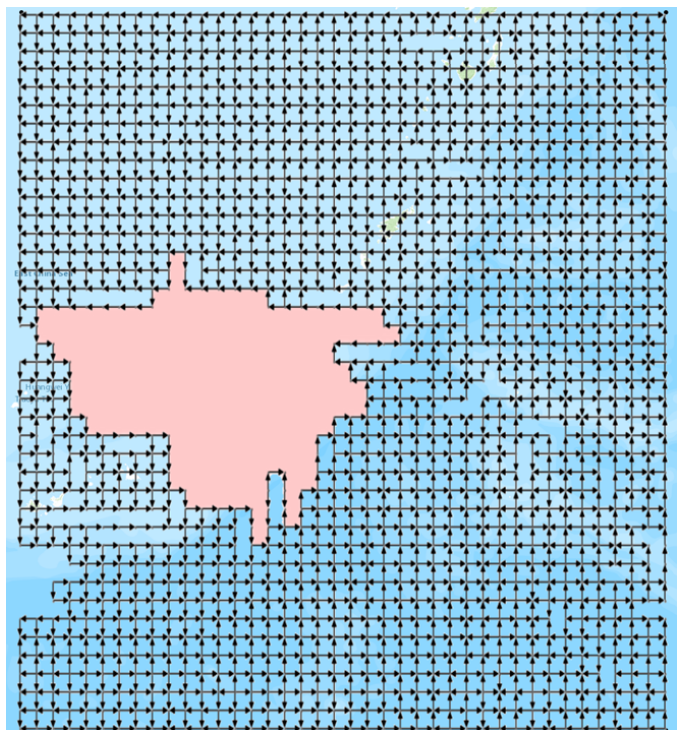


Fig. 10. Segmentation of singular polygon using the wind field data at 2023-08-02-00:00 UTC. The pink area shows the singular polygon that corresponds to the tropical cyclone center, which is an area influenced by the tropical cyclone.

our results with data of actual location provided by IGRF [38], as shown in Table II. It is evident that our method incurs only minor positioning errors, thus reaffirming its effectiveness. The positioning results are also plotted on maps (Fig. 11).

B. Vector Field Difference Measurement

In the following, we will use the wind field datasets as an example to demonstrate how our method can measure the variation of time-varying vector fields. Similar as the work [50], we will use the resulting persistence diagrams obtained by wind fields to measure the variations of singular patterns of the wind fields of the two tropical cyclones respectively.

Specifically, we sequentially compute the bottleneck distance between the persistence diagrams of two neighboring moments. The results are displayed in Fig. 12, where the point labeled k represents the bottleneck distance between the 1-dimensional persistence diagram at the $(k + 1)$ -th moment and the persistence diagram at the k -th moment. For instance, the first moment of Khanun is 2023-07-31-06:00 UTC; thus, the first blue point's value represents the bottleneck distance between the persistence diagram obtained at 2023-07-31-06:00 UTC and the one obtained at 2023-07-31-00:00 UTC. The first moment of Saola is 2023-08-25-06:00 UTC; hence, the first orange point's value represents the bottleneck distance between the persistence diagram obtained at 2023-08-25-06:00 UTC and the one obtained at 2023-08-25-00:00 UTC.

From blue line in Fig. 12, it is evident that the bottleneck distance reached a local minimum at the moment 2023-08-03-18:00 UTC, coinciding with the time when Khanun became

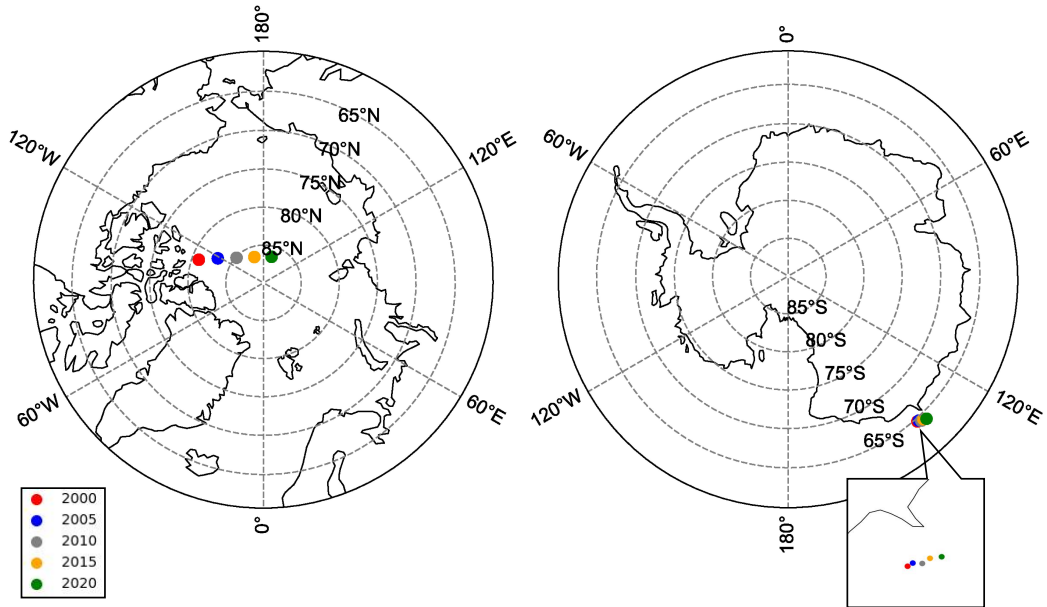


Fig. 11. The positioning results of north dip pole (left) and south dip pole (right) for the years 2000, 2005, 2010, 2015, and 2020.

stationary near a position since a notable change in trajectory was taking place. This period exhibited reduced variability in the wind field, resulting in a smaller difference between the persistence diagrams. Similarly, in orange line in Fig. 12, at the moment 2023-08-27-18:00 UTC, Saola became stationary near a position, where its trajectory was changing direction, indicating small variability between the persistence diagrams of the corresponding wind fields. Similar features of bottleneck distance can be observed at other moments, such as 2023-08-31-06:00 UTC, during which period Saola moves slowly within the vicinity of a location. Conversely, if a tropical cyclone undergoes significant movement or multiple turns over a period of time, the corresponding bottleneck distance will be larger. Moreover, a significant fluctuation of the bottleneck distance may indicate that the tropical cyclone is undergoing unstable movement and change.

Hence, considering our finding that the magnitude of the bottleneck distance between the corresponding persistence diagrams of the wind fields over a specific period reflects the extent of changes in the singular patterns of the tropical cyclones during that time, coupled with the widespread belief that these changes may result from the influence of various natural factors on the tropical cyclones, we also believe that our method can be applied to analyze the factors contributing to the variations in tropical cyclones.

C. Comparisons with State-of-the-art Methods

In this section, we will compare the mean positioning errors and running time between our method and several state-of-the-art methods. To calculate the mean errors, suppose that we have data for n moments, and we denote the i -th actual longitude as al_i and the i -th positioning longitude as pl_i . The mean longitude error can be computed using the formula $\frac{1}{n} \sum_{i=1}^n |al_i - pl_i|$, and the mean latitude error can

be computed similarly. Table III provide a comparison of the mean errors obtained using our method with some state-of-the-art singularity extraction methods, they are methods based on Hodge decomposition [24], triangular linear interpolation of vectors [25], and computation of the Jacobian matrix [26]. The average running times are also shown in Table III. The Khanun datasets consists of 1600 sampling vectors (resulting in a digraph of 1600 vertices and 3120 edges), the Saola datasets comprises 1924 sampling vectors (resulting in a digraph of 1924 vertices and 3759 edges), and the geomagnetic field datasets consists of 1600 sampling vectors (resulting in a digraph of 1600 vertices and 3120 edges). Based on the results, our method achieves smaller errors than the method proposed by [24], and its time cost is much shorter than [24]. Furthermore, our approach can achieve errors nearly as small as the numerical methods of [25] and [26], although it has a slightly longer time cost than those numerical methods. However, these numerical methods may fail to correctly identify singularities or encounter spurious singularities due to precision issues. For instance, in the experiments, both the triangular linear interpolation method and the Jacobian matrix method yield spurious singularities. The number of spurious singularities obtained from all vector fields in the corresponding datasets is shown in Table III. For example, in the geomagnetic field datasets, there are 10 vector fields and 10 corresponding singularities in total, but the triangular interpolation method finds 15 singularities, including 5 spurious singularities, and the Jacobian method finds 12 singularities, including 2 spurious singularities. In contrast, our method, which relies on the singularity index, finds all of the singularities without any spurious one. Additionally, our method has the capability to measure the variations between vector fields, while the other methods are unable to accomplish this.

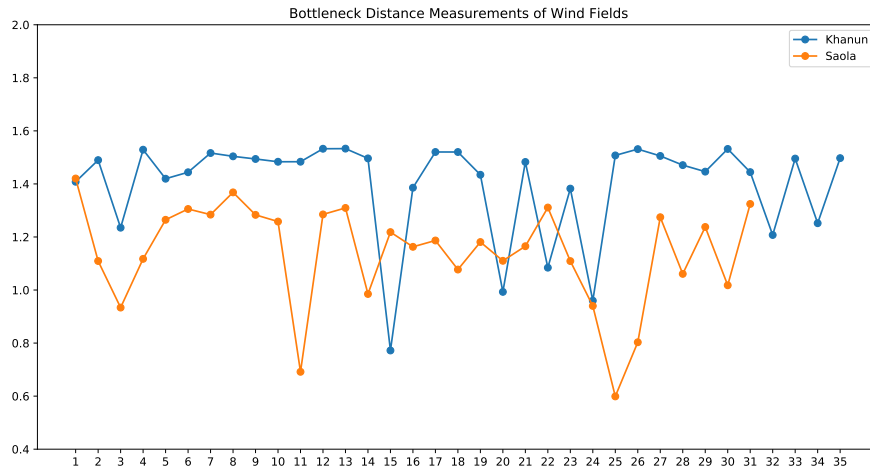


Fig. 12. Bottleneck distances computed by one-dimensional persistence diagrams derived from Khanun and Saola datasets respectively.

TABLE III
COMPARATIVE RESULTS

| Comparative Results for Khanun Datasets (36 vector fields) | | | | |
|---|-----------------------------------|----------------------------------|-----------------|----------------------|
| Method | Errors of longitude($^{\circ}$) | Errors of latitude($^{\circ}$) | Running time(s) | Spurious singularity |
| Triangular interpolation [25] | 0.134 | 0.107 | 27.21 | 15 |
| Jacobian method [26] | 0.126 | 0.109 | 45.25 | 9 |
| Hodge decomposition [24] | 0.205 | 0.147 | 566.64 | 0 |
| our method | 0.131 | 0.118 | 70.19 | 0 |
| Comparative Results for Saola Datasets (32 vector fields) | | | | |
| Method | Errors of longitude($^{\circ}$) | Errors of latitude($^{\circ}$) | Running time(s) | Spurious singularity |
| Triangular interpolation [25] | 0.108 | 0.093 | 34.76 | 15 |
| Jacobian method [26] | 0.111 | 0.093 | 56.00 | 2 |
| Hodge decomposition [24] | 0.129 | 0.133 | 689.39 | 0 |
| our method | 0.110 | 0.102 | 103.08 | 0 |
| Comparative Results for Geomagnetic Field Datasets (10 vector fields) | | | | |
| Method | Errors of longitude($^{\circ}$) | Errors of latitude($^{\circ}$) | Running time(s) | Spurious singularity |
| Triangular interpolation [25] | 0.028 | 0.056 | 27.90 | 5 |
| Jacobian method [26] | 0.030 | 0.000 | 47.31 | 2 |
| Hodge decomposition [24] | 0.089 | 0.182 | 572.02 | 0 |
| our method | 0.037 | 0.059 | 90.95 | 0 |

D. Discussion

Our method exhibits several limitations. If the sampling grid is not sufficiently dense, some singularities may not be extracted because multiple singularities may exist within the same square, and their indices can cancel each other out. Furthermore, singularities located on the edges of the grid digraph may be overlooked. In general, these situations are unlikely to occur due to practical considerations and limitations in numerical accuracy. However, new techniques should be developed to address these theoretical issues. Furthermore, the singular polygon may offer a coarse approximation of the singular pattern, given that the minimal cells in grid digraphs are square, implying that the boundary may not be smooth. Additionally, the existence of noise may cause a few edges to exist within the polygon, contradicting Theorem 5. For instance, in Fig. 10, even edges on the same line on the singular polygon may have different directions, although the proportion of such edges is minimal. Moreover, if the singularity and its corresponding singular pattern are located too close to the boundary of the considered region, the extraction of

the singular polygon may fail. Therefore, further refinement is required to obtain a more accurate representation of the region exhibiting the singular pattern.

VII. CONCLUSIONS

In this study, we propose a novel method for determining the position of a singularity and identifying the corresponding region of the singular pattern (referred to as the singular polygon) within a planar vector field exhibiting a singular pattern. Moreover, we compare the changes of singular patterns of time-varying vector fields using persistence diagrams. Our approach involves the conversion of discrete vector fields into angle-based grid digraphs, which are then analyzed using persistent path homology. Experimental results demonstrate that our proposed method achieves low mean errors in locating the centers of tropical cyclones and locations of dip poles, and effectively measures the changes in tropical cyclone features over time. Additionally, we can obtain the regions where singular patterns are present.

In future work, we aim to explore alternative techniques for converting vector fields into digraphs to accommodate diverse

applications, as well as more precise methods for extracting singular patterns. Furthermore, we will address challenges related to vector fields in higher dimensional Euclidean spaces or surfaces and investigate the potential utilization of higher dimensional (persistent) path homology as a new analytical tool.

ACKNOWLEDGMENTS

This work is supported by the National Natural Science Foundation of China under Grant nos. 62272406, 61972316. CCMP Version-3.0 vector wind analyses are produced by Remote Sensing Systems. Data are available at www.remss.com.

REFERENCES

- [1] K. Y. Wong and C. L. Yip, "Identifying centers of circulating and spiraling vector field patterns and its applications," *Pattern Recognition*, vol. 42, no. 7, pp. 1371–1387, Jul. 2009.
- [2] Hongyu Li, Wenbin Chen, and I-Fan Shen, "Segmentation of discrete vector fields," *IEEE Transactions on Visualization and Computer Graphics*, vol. 12, no. 3, pp. 289–300, May 2006.
- [3] A. Grigor'yan, Y. Lin, Y. Muranov, and S.-T. Yau, "Homologies of path complexes and digraphs," May 2013, arXiv:1207.2834 [math].
- [4] H. Edelsbrunner and J. Harer, "Persistent homology—a survey," in *Contemporary Mathematics*, J. E. Goodman, J. Pach, and R. Pollack, Eds. Providence, Rhode Island: American Mathematical Society, 2008, vol. 453, pp. 257–282.
- [5] A. Zomorodian and G. Carlsson, "Computing persistent homology," in *Proceedings of the twentieth annual symposium on Computational geometry*. Brooklyn New York USA: ACM, Jun. 2004, pp. 347–356.
- [6] Edelsbrunner, Letscher, and Zomorodian, "Topological Persistence and Simplification," *Discrete & Computational Geometry*, vol. 28, no. 4, pp. 511–533, Nov. 2002.
- [7] A. Grigor'yan, Y. Lin, Y. Muranov, and S.-T. Yau, "Homotopy theory for digraphs," *arXiv preprint arXiv:1407.0234*, 2014.
- [8] Y. Lin, C. Wang, and S.-T. Yau, "Discrete morse theory on digraphs," *arXiv preprint arXiv:2102.10518*, 2021.
- [9] A. Grigor'yan, Y. Muranov, V. Vershinin, and S.-T. Yau, "Path homology theory of multigraphs and quivers," in *Forum mathematicum*, vol. 30, no. 5. De Gruyter, 2018, pp. 1319–1337.
- [10] S. Chowdhury and F. Mémoli, "Persistent Path Homology of Directed Networks," in *Proceedings of the 2018 Annual ACM-SIAM Symposium on Discrete Algorithms (SODA)*, pp. 1152–1169.
- [11] T. K. Dey, T. Li, and Y. Wang, "An Efficient Algorithm for 1-Dimensional (Persistent) Path Homology," *Discrete & Computational Geometry*, vol. 68, no. 4, pp. 1102–1132, Dec. 2022.
- [12] S. Chowdhury, T. Gebhart, S. Huntsman, and M. Yutin, "Path homologies of deep feedforward networks," in *2019 18th IEEE International Conference On Machine Learning And Applications (ICMLA)*. IEEE, 2019, pp. 1077–1082.
- [13] D. Chen, J. Liu, J. Wu, G.-W. Wei, F. Pan, and S.-T. Yau, "Path topology in molecular and materials sciences," *The journal of physical chemistry letters*, vol. 14, no. 4, pp. 954–964, 2023.
- [14] J. Liu, D. Chen, F. Pan, and J. Wu, "Neighborhood path complex for the quantitative analysis of the structure and stability of carboranes," *Journal of Computational Biophysics and Chemistry*, vol. 22, no. 04, pp. 503–511, 2023.
- [15] S. Wu, X. Liu, A. Dong, C. Gagnoli, C. Griffin, J. Wu, S.-T. Yau, and R. Wu, "The metabolomic physics of complex diseases," *Proceedings of the National Academy of Sciences*, vol. 120, no. 42, p. e2308496120, 2023.
- [16] J. L. Helman and L. Hesselink, "Visualizing vector field topology in fluid flows," *IEEE Computer Graphics and Applications*, vol. 11, no. 3, pp. 36–46, 1991.
- [17] F. H. Post, B. Vrolijk, H. Hauser, R. S. Laramée, and H. Doleisch, "The state of the art in flow visualisation: Feature extraction and tracking," in *Computer Graphics Forum*, vol. 22, no. 4. Wiley Online Library, 2003, pp. 775–792.
- [18] R. S. Laramée, H. Hauser, L. Zhao, and F. H. Post, "Topology-based flow visualization, the state of the art," *Topology-based methods in visualization*, pp. 1–19, 2007.
- [19] T. Salzbrunn, H. Janicke, T. Wischgoll, and G. Scheuermann, "The state of the art in flow visualization: Partition-based techniques," 2008.
- [20] A. Pobitzer, R. Peikert, R. Fuchs, B. Schindler, A. Kuhn, H. Theisel, K. Matković, and H. Hauser, "The state of the art in topology-based visualization of unsteady flow," in *Computer Graphics Forum*, vol. 30, no. 6. Wiley Online Library, 2011, pp. 1789–1811.
- [21] T. Günther and H. Theisel, "The state of the art in vortex extraction," in *Computer Graphics Forum*, vol. 37, no. 6. Wiley Online Library, 2018, pp. 149–173.
- [22] A. A. Andronov, E. A. Leontovich, I. I. Gordon, A. G. Maier, and M. C. Gutzwiller, "Qualitative Theory of Second-Order Dynamic Systems," *Physics Today*, vol. 27, no. 8, pp. 53–54, Aug. 1974.
- [23] Y. Tong, S. Lombeyda, A. N. Hirani, and M. Desbrun, "Discrete multiscale vector field decomposition," *ACM Transactions on Graphics*, vol. 22, no. 3, pp. 445–452, Jul. 2003.
- [24] K. Polthier and E. Preuß, "Identifying Vector Field Singularities Using a Discrete Hodge Decomposition," in *Visualization and Mathematics III*, G. Farin, H.-C. Hege, D. Hoffman, C. R. Johnson, K. Polthier, H.-C. Hege, and K. Polthier, Eds. Berlin, Heidelberg: Springer Berlin Heidelberg, 2003, pp. 113–134, series Title: Mathematics and Visualization.
- [25] X. Tricoche, T. Wischgoll, G. Scheuermann, and H. Hagen, "Topology tracking for the visualization of time-dependent two-dimensional flows," *Computers & Graphics*, vol. 26, no. 2, pp. 249–257, 2002.
- [26] T. Weinkauff, "Extraction of topological structures in 2d and 3d vector fields," Ph.D. dissertation, Magdeburg, Univ., Diss., 2008.
- [27] J.-L. Chen, Z. Bai, B. Hamann, and T. J. Ligocki, "Normalized-cut algorithm for hierarchical vector field data segmentation," R. F. Erbacher, P. C. Chen, J. C. Roberts, M. T. Groehn, and K. Boerner, Eds., Santa Clara, CA, May 2003, pp. 79–90.
- [28] L. Zhang, R. S. Laramée, D. Thompson, A. Sescu, and G. Chen, "An integral curve attribute based flow segmentation," *Journal of Visualization*, vol. 19, no. 3, pp. 423–436, Aug. 2016.
- [29] J. Daniels, E. W. Anderson, L. G. Nonato, and C. T. Silva, "Interactive Vector Field Feature Identification," *IEEE Transactions on Visualization and Computer Graphics*, vol. 16, no. 6, pp. 1560–1568, Nov. 2010.
- [30] H. Theisel, C. Rössl, and H.-P. Seidel, "Using feature flow fields for topological comparison of vector fields," in *International Symposium on Vision, Modeling, and Visualization*, 2003.
- [31] M. Jiang, R. Machiraju, and D. Thompson, "Detection and visualization of vortices," *The visualization handbook*, vol. 295, 2005.
- [32] D. Cohen-Steiner, H. Edelsbrunner, and J. Harer, "Stability of persistence diagrams," in *Proceedings of the Twenty-First Annual Symposium on Computational Geometry*, ser. SCG '05. New York, NY, USA: Association for Computing Machinery, 2005, p. 263–271. [Online]. Available: <https://doi.org/10.1145/1064092.1064133>
- [33] F. Chazal, D. Cohen-Steiner, L. J. Guibas, and S. Oudot, "The stability of persistence diagrams revisited," 2008.
- [34] D. Cohen-Steiner, H. Edelsbrunner, J. Harer, and Y. Mileyko, "Lipschitz functions have 1-p-stable persistence," *Foundations of computational mathematics*, vol. 10, no. 2, pp. 127–139, 2010.
- [35] X. Tricoche, G. Scheuermann, and H. Hagen, "Continuous topology simplification of planar vector fields," in *Proceedings Visualization, 2001. VIS '01*. San Diego, CA, USA: IEEE, 2001, pp. 159–166.
- [36] T. K. Dey, T. Hou, and S. Mandal, "Persistent 1-cycles: Definition, computation, and its application," in *Computational Topology in Image Context: 7th International Workshop, CTIC 2019, Málaga, Spain, January 24–25, 2019, Proceedings 7*. Springer, 2019, pp. 123–136.
- [37] Remote Sensing Systems, C. Mears, T. Lee, L. Ricciardulli, X. Wang, and F. Wentz, "RSS Cross-Calibrated Multi-Platform (CCMP) 6-hourly ocean vector wind analysis on 0.25 deg grid, Version 3.0," Aug. 2022, institution: Remote Sensing Systems. [Online]. Available: <https://www.remss.com/DOI/RSS-uv6h30.html>
- [38] P. Alken, E. Thébault, C. D. Beggan, H. Amit, J. Aubert, J. Baerenzung, T. Bondar, W. Brown, S. Califf, A. Chambodut *et al.*, "International geomagnetic reference field: the thirteenth generation," *Earth, Planets and Space*, vol. 73, pp. 1–25, 2021.
- [39] U. Neu, M. G. Akperov, N. Bellenbaum, R. Benestad, R. Blender, R. Caballero, A. Coccozza, H. F. Dacre, Y. Feng, K. Fraedrich *et al.*, "Imilast: A community effort to intercompare extratropical cyclone detection and tracking algorithms," *Bulletin of the American Meteorological Society*, vol. 94, no. 4, pp. 529–547, 2013.
- [40] Zhengguang Liu, Bing Wu, Juntao Xue, and Huanzhu Liu, "The non-eye typhoon center locating with parallel computing," in *Proceedings of the 8th International Scientific and Practical Conference of Students, Post-graduates and Young Scientists. Modern Technique and Technologies*.

- MTT'2002 (Cat. No.02EX550)*. Chengdu, China: IEEE, 2003, pp. 488–491.
- [41] J. Yang and H. Wang, “Positioning Tropical Cyclone Center in a Single Satellite Image Using Vector Field Analysis,” in *Proceedings of 2013 Chinese Intelligent Automation Conference*, Z. Sun and Z. Deng, Eds. Berlin, Heidelberg: Springer Berlin Heidelberg, 2013, vol. 256, pp. 37–44, series Title: Lecture Notes in Electrical Engineering.
- [42] T.-L. Pao, J.-H. Yeh, M.-Y. Liu, and Y.-C. Hsu, “Locating the Typhoon Center from the IR Satellite Cloud Images,” in *2006 IEEE International Conference on Systems, Man and Cybernetics*. Taipei, Taiwan: IEEE, Oct. 2006, pp. 484–488.
- [43] G. Yin and Y. F. Chen, “A New Algorithm of Eyed Typhoon Automatic Positioning Based on Single Infrared Satellite Cloud Image,” *Applied Mechanics and Materials*, vol. 347-350, pp. 3809–3814, Aug. 2013.
- [44] Jun-Heng Yeh, Tsang-Long Pao, Chung-Lang Lee, and Wei-Ta Lai, “Reconstruction of typhoon path and cloud image from descriptors,” in *2007 IEEE International Conference on Systems, Man and Cybernetics*. Montreal, QC, Canada: IEEE, 2007, pp. 2097–2101.
- [45] Ping Wang, Pei-Long Yang, Wen-Li Li, and Han-Qing Lu, “Extracting the rotation feature of the developing typhoon,” in *2005 International Conference on Machine Learning and Cybernetics*. Guangzhou, China: IEEE, 2005, pp. 5229–5234 Vol. 8.
- [46] L. Yan, H. Guo, T. Peterka, B. Wang, and J. Wang, “Trophy: A topologically robust physics-informed tracking framework for tropical cyclones,” *IEEE Transactions on Visualization and Computer Graphics*, 2023.
- [47] W. Engelke, T. B. Masood, J. Beran, R. Caballero, and I. Hotz, “Topology-based feature design and tracking for multi-center cyclones,” in *Topological Methods in Data Analysis and Visualization VI: Theory, Applications, and Software*. Springer, 2021, pp. 71–85.
- [48] X. Yang, Z. Zhan, and J. Shen, “A Deep Learning Based Method for Typhoon Recognition and Typhoon Center Location,” in *IGARSS 2019 - 2019 IEEE International Geoscience and Remote Sensing Symposium*. Yokohama, Japan: IEEE, Jul. 2019, pp. 9871–9874.
- [49] C. Tan, “TCLNet: Learning to Locate Typhoon Center using Deep Neural Network,” in *2021 IEEE International Geoscience and Remote Sensing Symposium IGARSS*. Brussels, Belgium: IEEE, Jul. 2021, pp. 4600–4603.
- [50] M. Soler, M. Plainchault, B. Conche, and J. Tierny, “Lifted wasserstein matcher for fast and robust topology tracking,” *2018 IEEE 8th Symposium on Large Data Analysis and Visualization (LDAV)*, pp. 23–33, 2018.

TABLE IV
 POSITIONING RESULTS AND ERRORS OF THE CENTER TRACKING. FROM 2023/07/31 TO 2023/08/08 ARE RESULTS OF KHANUN; FROM 2023/08/25 TO 2023/09/01 ARE RESULTS OF SAOLA

| UTC | Actual longitude(E) | Actual latitude(N) | Positioning longitude(E) | Positioning latitude(N) | Errors of longitude | Errors of latitude |
|------------------|---------------------|--------------------|--------------------------|-------------------------|---------------------|--------------------|
| 2023/07/31/00:00 | 132 | 22.1 | 131.99 | 22.22 | 0.01 | 0.12 |
| 2023/07/31/06:00 | 131.5 | 22.8 | 131.52 | 23 | 0.02 | 0.2 |
| 2023/07/31/12:00 | 131.1 | 23.4 | 130.99 | 23.29 | 0.11 | 0.11 |
| 2023/07/31/18:00 | 130.3 | 24 | 130.03 | 24.25 | 0.27 | 0.25 |
| 2023/08/01/00:00 | 129.4 | 24.6 | 129.27 | 24.51 | 0.13 | 0.09 |
| 2023/08/01/06:00 | 128.7 | 25 | 128.52 | 24.97 | 0.18 | 0.03 |
| 2023/08/01/12:00 | 128 | 25.3 | 127.77 | 25.22 | 0.23 | 0.08 |
| 2023/08/01/18:00 | 127.4 | 25.6 | 127.26 | 25.5 | 0.14 | 0.1 |
| 2023/08/02/00:00 | 126.8 | 25.7 | 126.78 | 25.75 | 0.02 | 0.05 |
| 2023/08/02/06:00 | 126.1 | 26 | 126 | 26.03 | 0.1 | 0.03 |
| 2023/08/02/12:00 | 125.6 | 26.2 | 125.52 | 26.02 | 0.08 | 0.18 |
| 2023/08/02/18:00 | 125.1 | 26.4 | 125.03 | 26.28 | 0.07 | 0.12 |
| 2023/08/03/00:00 | 124.8 | 26.7 | 124.77 | 26.53 | 0.03 | 0.17 |
| 2023/08/03/06:00 | 124.3 | 26.7 | 124.3 | 26.74 | 0 | 0.04 |
| 2023/08/03/12:00 | 124.1 | 26.9 | 124.26 | 26.72 | 0.16 | 0.18 |
| 2023/08/03/18:00 | 124.2 | 26.8 | 124.26 | 26.78 | 0.06 | 0.02 |
| 2023/08/04/00:00 | 124.5 | 27 | 124.72 | 27.02 | 0.22 | 0.02 |
| 2023/08/04/06:00 | 125.2 | 27.2 | 125.21 | 27.25 | 0.01 | 0.05 |
| 2023/08/04/12:00 | 125.7 | 27.5 | 125.73 | 27.49 | 0.03 | 0.01 |
| 2023/08/04/18:00 | 126.3 | 27.6 | 126.23 | 27.55 | 0.07 | 0.05 |
| 2023/08/05/00:00 | 126.9 | 27.7 | 126.75 | 27.77 | 0.15 | 0.07 |
| 2023/08/05/06:00 | 127.6 | 27.8 | 127.75 | 27.97 | 0.15 | 0.17 |
| 2023/08/05/12:00 | 128.4 | 27.9 | 128.47 | 27.78 | 0.07 | 0.12 |
| 2023/08/05/18:00 | 129 | 27.9 | 128.96 | 28.22 | 0.04 | 0.32 |
| 2023/08/06/00:00 | 129.4 | 27.8 | 129.5 | 28.2 | 0.1 | 0.4 |
| 2023/08/06/06:00 | 130 | 27.7 | 129.98 | 27.51 | 0.02 | 0.19 |
| 2023/08/06/12:00 | 130.5 | 27.5 | 130.3 | 27.46 | 0.2 | 0.04 |
| 2023/08/06/18:00 | 130.8 | 27.7 | 130.77 | 27.72 | 0.03 | 0.02 |
| 2023/08/07/00:00 | 131 | 27.8 | 131.25 | 27.75 | 0.25 | 0.05 |
| 2023/08/07/06:00 | 131.1 | 27.9 | 131.26 | 27.98 | 0.16 | 0.08 |
| 2023/08/07/12:00 | 131.3 | 28.2 | 131 | 28.24 | 0.3 | 0.04 |
| 2023/08/07/18:00 | 131.1 | 28.4 | 130.75 | 28.54 | 0.35 | 0.14 |
| 2023/08/08/00:00 | 130.9 | 29 | 131.04 | 29.24 | 0.14 | 0.24 |
| 2023/08/08/06:00 | 130.8 | 29.3 | 130.78 | 29.53 | 0.02 | 0.23 |
| 2023/08/08/12:00 | 130.4 | 29.9 | 130 | 29.78 | 0.4 | 0.12 |
| 2023/08/08/18:00 | 129.7 | 30.4 | 129.29 | 30.53 | 0.41 | 0.13 |
| 2023/08/25/00:00 | 124 | 19.7 | 124.26 | 19.99 | 0.26 | 0.29 |
| 2023/08/25/06:00 | 123.9 | 19.7 | 124.25 | 19.52 | 0.35 | 0.18 |
| 2023/08/25/12:00 | 123.6 | 19.5 | 123.96 | 19.26 | 0.36 | 0.24 |
| 2023/08/25/18:00 | 123.4 | 19.3 | 123.53 | 19.22 | 0.13 | 0.08 |
| 2023/08/26/00:00 | 123.2 | 18.5 | 123.26 | 18.71 | 0.06 | 0.21 |
| 2023/08/26/06:00 | 123.2 | 18 | 123.28 | 18 | 0.08 | 0 |
| 2023/08/26/12:00 | 123.1 | 17.6 | 123.02 | 17.52 | 0.08 | 0.08 |
| 2023/08/26/18:00 | 122.9 | 17.2 | 123.04 | 17.24 | 0.14 | 0.04 |
| 2023/08/27/00:00 | 122.9 | 16.8 | 123 | 16.77 | 0.1 | 0.03 |
| 2023/08/27/06:00 | 123 | 16.5 | 122.97 | 16.49 | 0.03 | 0.01 |
| 2023/08/27/12:00 | 123.2 | 16.3 | 123.28 | 16.23 | 0.08 | 0.07 |
| 2023/08/27/18:00 | 123.8 | 16 | 123.74 | 16.21 | 0.06 | 0.21 |
| 2023/08/28/00:00 | 124.3 | 16.8 | 124.27 | 16.51 | 0.03 | 0.29 |
| 2023/08/28/06:00 | 124.3 | 17.5 | 124.26 | 17.48 | 0.04 | 0.02 |
| 2023/08/28/12:00 | 124.1 | 17.8 | 124.25 | 17.75 | 0.15 | 0.05 |
| 2023/08/28/18:00 | 123.9 | 18.2 | 124 | 18.22 | 0.1 | 0.02 |
| 2023/08/29/00:00 | 123.5 | 18.6 | 123.51 | 18.51 | 0.01 | 0.09 |
| 2023/08/29/06:00 | 123.1 | 18.9 | 123 | 18.76 | 0.1 | 0.14 |
| 2023/08/29/12:00 | 122.7 | 19.3 | 122.51 | 19.29 | 0.19 | 0.01 |
| 2023/08/29/18:00 | 121.9 | 19.9 | 121.96 | 19.73 | 0.06 | 0.17 |
| 2023/08/30/00:00 | 121.1 | 20.1 | 121.23 | 20 | 0.13 | 0.1 |
| 2023/08/30/06:00 | 120.4 | 20.4 | 120.46 | 20.49 | 0.06 | 0.09 |
| 2023/08/30/12:00 | 119.7 | 20.7 | 119.51 | 20.71 | 0.19 | 0.01 |
| 2023/08/30/18:00 | 118.7 | 20.9 | 118.99 | 20.96 | 0.29 | 0.06 |
| 2023/08/31/00:00 | 118.2 | 21 | 118.22 | 21 | 0.02 | 0 |
| 2023/08/31/06:00 | 117.8 | 21.2 | 117.74 | 21.26 | 0.06 | 0.06 |
| 2023/08/31/12:00 | 117.3 | 21.5 | 117.25 | 21.47 | 0.05 | 0.03 |
| 2023/08/31/18:00 | 116.8 | 21.7 | 116.99 | 21.54 | 0.19 | 0.16 |
| 2023/09/01/00:00 | 116.3 | 21.9 | 116.22 | 21.97 | 0.08 | 0.07 |
| 2023/09/01/06:00 | 115.5 | 22 | 115.5 | 21.78 | 0 | 0.22 |
| 2023/09/01/12:00 | 114.5 | 22 | 114.52 | 22.01 | 0.02 | 0.01 |
| 2023/09/01/18:00 | 113.5 | 22 | 113.49 | 21.77 | 0.01 | 0.23 |

APPENDIX
PROOF OF THE THEOREM 5

Proof. A number of singular patterns such as sources, sinks, circulating and spiraling vector fields can be modeled or approximated by a field generated by logarithmic spirals [1]. The formula of each grid point can be described by

$$\begin{cases} x = ae^{\theta \cot \alpha} \cos \theta \\ y = \frac{a}{\rho} e^{\theta \cot \alpha} \sin \theta \end{cases}$$

and the vector located on (x, y) is

$$\begin{cases} P = ae^{\theta \cot \alpha} (\cot \alpha \cos \theta - \sin \theta) = x \cot \alpha - \rho y \\ Q = \frac{a}{\rho} e^{\theta \cot \alpha} (\cot \alpha \sin \theta + \cos \theta) = y \cot \alpha + \frac{x}{\rho} \end{cases}$$

where θ is the polar angle, $\alpha \in [0, \pi)$ is the angle between the radial line and the tangent of the spiral at (r, θ) ; parameter a is non-zero, and a counterclockwise field is generated by a positive a while a clockwise field is generated by a negative a ; parameter ρ controls the width-to-height ratio.

To prove this theorem, we only need to consider the case of a horizontal line, as the vertical case can be proven similarly. Without loss of generality, let us assume that the singularity is located at $O(0, 0)$. Suppose (x, y) and $(x + \varepsilon, y)$ are two points in U , which can be described in polar coordinates as follows:

$$\begin{aligned} x &= a_1 e^{\theta_1 \cot \alpha_1} \cos \theta_1, & x + \varepsilon &= b_1 e^{\theta_2 \cot \alpha_2} \cos \theta_2 \\ y &= \frac{a_1}{\rho} e^{\theta_1 \cot \alpha_1} \sin \theta_1 = \frac{b_1}{\rho} e^{\theta_2 \cot \alpha_2} \sin \theta_2 \end{aligned}$$

Here, $a_1, b_1, \theta_1, \theta_2, \alpha_1, \alpha_2$ and ρ are constants such that $y \neq 0$, with a_1 and b_1 both positive or negative. By rewriting the equation, we have:

$$\begin{aligned} b_1 e^{\theta_2 \cot \alpha_2} &= b_1 e^{\theta_2 (\cot \alpha_2 - \cot \alpha_1 + \cot \alpha_1)} \\ &= (b_1 e^{\theta_2 (\cot \alpha_2 - \cot \alpha_1)}) e^{\theta_2 \cot \alpha_1} \end{aligned}$$

Let $a_2 = b_1 e^{\theta_2 (\cot \alpha_2 - \cot \alpha_1)}$ and $\alpha = \alpha_1$. Then, we can express $x, x + \varepsilon, y$ as:

$$\begin{aligned} x &= a_1 e^{\theta_1 \cot \alpha} \cos \theta_1, & x + \varepsilon &= a_2 e^{\theta_2 \cot \alpha} \cos \theta_2 \\ y &= \frac{a_1}{\rho} e^{\theta_1 \cot \alpha} \sin \theta_1 = \frac{a_2}{\rho} e^{\theta_2 \cot \alpha} \sin \theta_2 \end{aligned}$$

Note that a_2 and α are also constants. Therefore, ε can be written as:

$$\begin{aligned} \varepsilon &= a_2 e^{\theta_2 \cot \alpha} \cos \theta_2 - a_1 e^{\theta_1 \cot \alpha} \cos \theta_1 \\ &= a_2 e^{\theta_2 \cot \alpha} \cos \theta_2 - a_2 e^{\theta_2 \cot \alpha} \frac{\sin \theta_2}{\sin \theta_1} \cos \theta_1 \\ &= a_2 e^{\theta_2 \cot \alpha} \frac{\sin(\theta_1 - \theta_2)}{\sin \theta_1} \end{aligned}$$

Now, let's define:

$$\begin{aligned} X_1 &= (P(x, y), Q(x, y), 0) \\ &= (x \cot \alpha - \rho y, y \cot \alpha + \frac{x}{\rho}, 0) \\ X_2 &= (P(x + \varepsilon, y), Q(x + \varepsilon, y), 0) \\ &= ((x + \varepsilon) \cot \alpha - \rho y, y \cot \alpha + \frac{x + \varepsilon}{\rho}, 0) \end{aligned}$$

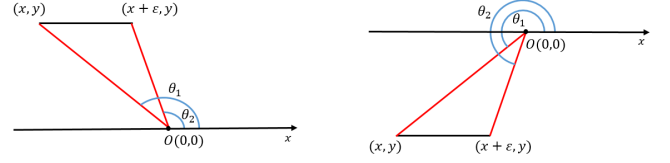


Fig. 13. (left) Situation of $y > 0$; (right) Situation of $y < 0$.

Thus, the third component of $X_2 \times X_1$ is given by:

$$\begin{aligned} z &= ((x + \varepsilon) \cot \alpha - \rho y) (y \cot \alpha + \frac{x}{\rho}) \\ &\quad - (x \cot \alpha - \rho y) (y \cot \alpha + \frac{x + \varepsilon}{\rho}) \\ &= \varepsilon y (1 + \cot^2 \alpha) \\ &= a_2 y (1 + \cot^2 \alpha) e^{\theta_2 \cot \alpha} \frac{\sin(\theta_1 - \theta_2)}{\sin \theta_1} \end{aligned}$$

If $y > 0$, then θ_1 and θ_2 lie in the interval $(0, \pi)$, and $\sin(\theta_1 - \theta_2) > 0$ and $\sin \theta_1 > 0$ (see left part in Fig. 13), thus z has the same sign as a_2 . If $y < 0$, then θ_1 and θ_2 lie in the interval $(\pi, 2\pi)$, and $\sin(\theta_1 - \theta_2) < 0$ and $\sin \theta_1 < 0$ (see right part in Fig. 13), thus z has the opposite sign of a_2 . Since the choice of x, y , and ε is arbitrary, the sign of z only depends on the sign of y and a_2 , leading to our conclusion. \square